Spin Detection via Parametric Frequency Conversion in a Membrane Resonator

Jan Košata,[1,*] Oded Zilberberg,[1] Christian L. Degen,[2] R. Chitra,[1] and Alexander Eichler[2]

[1] *Institute for Theoretical Physics, ETH Zürich, Zürich 8093, Switzerland*

[2] *Laboratory for Solid State Physics, ETH Zürich, Zürich 8093, Switzerland*

(Received 6 March 2020; revised 22 May 2020; accepted 16 June 2020; published 15 July 2020)

Recent demonstrations of ultracoherent nanomechanical resonators introduce the prospect of developing protocols for solid-state sensing applications. Here, we propose to use two coupled ultracoherent resonator modes on a Si_3N_4 membrane for the detection of small nuclear spin ensembles. To this end, we employ parametric frequency conversion between nondegenerate modes. The nondegenerate modes result from coupled degenerate resonators, and the parametric conversion is mediated by periodic inversions of the nuclear spins in the presence of a magnetic scanning tip. We analyze potential noise sources and derive the achievable signal-to-noise ratio with typical experimental parameter values. Our proposal reconciles the geometric constraints of optomechanical systems with the requirements of scanning force microscopy and brings forth a promising platform for spin-phonon interaction and spin imaging.

DOI: 10.1103/PhysRevApplied.14.014042

I. INTRODUCTION

Nanoscale magnetic resonance imaging (nano-MRI) aims at detecting nuclear spins in three spatial dimensions with subnanometer resolution [1–6]. In contrast to other techniques like electron microscopy or x-ray tomography, nano-MRI is able to obtain three-dimensional (3D) images of complex macromolecules in a nondestructive manner. Combined with the elemental selectivity of MRI, this emerging technique has the potential to become a unique probe of the 3D composition of nanostructures.

Achieving the necessary sensitivity to detect the magnetic moment of a nanometer-sized nuclear spin ensemble is a formidable task. One candidate technique to achieve this goal is magnetic resonance force microscopy (MRFM) [1,2,7–11]. In MRFM, nuclear spins are periodically inverted inside a magnetic field gradient to generate a force proportional to the spin magnetic moment. A mechanical transducer is used to detect this force and to translate it into an optical or electrical signal. The sensitivity of the transducer is typically limited by the thermomechanical force noise power spectral density (PSD) of its resonant mode,

$$S_f = 4k_B T\gamma, \tag{1}$$

where k_B is the Boltzmann constant and T is the mode temperature. The transducer's dissipation coefficient is $\gamma = \sqrt{mk}/Q = m\omega_0/Q$, where m is the effective mass of the mode, $\omega_0 = 2\pi f_0$ is the angular resonance frequency, $k = m\omega_0^2$ is the spring constant, and Q is the mechanical quality factor. In order to reach better sensitivity, much effort is being invested to reduce the dissipation [12–23].

Traditional MRFM setups are constructed around cantilever resonators with very small spring constants [8–12,18,21]. While this strategy reduces γ, it can generate issues with long-term stability and strong tip-sample interaction. In addition, one of the primary goals of MRFM is the imaging of biological samples and macromolecules, which are difficult to mount on the tip of a cantilever. Recently, a route towards ultra-low damping coefficients has emerged through the development of soft-clamped silicon nitride membranes and strings, with localized defect modes that feature quality factors up to the $Q \sim 10^9$ range [20,23,24]. Thanks to this outstanding virtue, silicon nitride resonators offer force sensitivities comparable to those of singly clamped cantilevers, in spite of their higher masses and resonance frequencies.

Silicon nitride membranes are attractive transducers for spin detection instruments [25–28]. Their large surface allows simple placement of samples, and their high spring constants ensure low displacement drift and bending even in the proximity of a scanning tip. However, there remains one serious obstacle, which we term the "frequency mismatch problem": the vibrational modes of interest are in the low megahertz range. Inverting nuclear spins adiabatically at an angular rate of $2\omega_0$, as required by traditional MRFM protocols [1,2], is unrealistic with such devices. More specifically, current experiments use oscillating fields of a few millitesla in amplitude to achieve inversion rates of approximately 10 kHz [29]. Scaling this method to megahertz frequencies would entail oscillating

*kosataj@phys.ethz.ch

field amplitudes that are incompatible with cryogenic operation and nanoscale precision.

In this paper, we propose a sensing scheme that circumvents the frequency mismatch problem. We employ a parametric up-conversion method [30,31] to couple two nondegenerate normal modes. The coupling is achieved by a modulation of the effective mechanical frequencies via nuclear spins that are inverted at the splitting frequency. We explore how degenerate local defect modes on the membrane give rise to split extended normal modes, how parametric modulation of a local mode leads to coupling between the normal modes, and how parametric modulation is generated by nuclear spins placed on one local mode in the presence of a magnetic field gradient source. In addition to solving the frequency mismatch problem, the extended nature of the normal modes allows for spatial separation of the sample placement and the readout of the membrane vibrations. This facilitates the integration of our proposed scanning force setup into a high-finesse optical cavity, which allows very sensitive readout of the membrane vibrations and enables a host of optomechanical control techniques [32]. From our analysis with realistic experimental parameters, we currently predict a sensitivity competitive with that of contemporary cantilever-based MRFM [10,11,29,33], while harnessing the advantages of the membrane platform (these we discuss in more detail in Sec. VII B). Furthermore, we pinpoint the critical properties of the resonator to design transducers with improved spin detection performances in the future.

The working principle of our sensing scheme is outlined in Sec. II. In Sec. III, we derive the full equation of motion for the system in the coupled mode basis. In Sec. IV, we obtain a simple closed-form expression for the signal gain in the absence of nonlinearities and noise. The limitations of this scheme due to the onset of nonlinear behavior are explored in Sec. V, followed by noise analysis and a derived expression for the signal-to-noise ratio in Sec. VI. Finally, in Sec. VII we present a survey of current state-of-the-art experimental possibilities and evaluate the expected performance of our method.

II. GENERAL IDEA

We now present our spin detection scheme based on membrane transducers. Consider an elastic membrane patterned with a hexagonal array of holes (see Fig. 1) to create a phononic band gap [20]. Small defects in the pattern define localized out-of-plane vibrational modes whose frequencies lie within the gap—these modes are effectively isolated from the rest of the membrane and can thus reach extremely high quality factors.

We consider two such modes with equal frequencies and effective masses. When in close proximity, the modes are mechanically coupled, giving rise to symmetric and antisymmetric normal modes with frequencies $\omega_S = \omega_0$ and

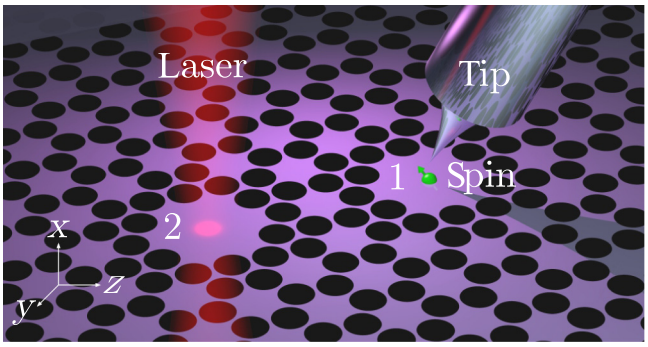

FIG. 1. Proposed measurement setup. A silicon nitride membrane is patterned such that a phononic bandstructure is obtained with explicit band gaps. Two unpatterned "defect" areas define in-gap vibrational modes (labeled 1 and 2). A sample spin (or an ensemble of spins) on defect 1 is periodically inverted by radio-frequency pulses, while a sharp tip provides a magnetic field gradient, transducing the spin inversion to a force acting on the membrane. A cavity laser focused on defect 2 is used for driving and readout. Each hole in the pattern has a diameter of roughly 80 μm.

$\omega_A > \omega_S$ [see Figs. 2(a) and 2(b)] [34]. The frequencies ω_S and ω_A are in the megahertz range, but their difference $\Delta\omega = \omega_A - \omega_S$ is on the order of a few kilohertz.

An ensemble of spins with magnetization M is placed on one of the defects and is periodically inverted by radio-frequency pulses [2]. In the presence of a magnetic tip, the magnetic field gradient couples mechanical motion to the spin moment. Namely, the second derivative leads to a frequency modulation of the corresponding defect mode. This modulation translates into a time-dependent coupling between the normal modes [35]. If this coupling is periodically varied exactly at the rate $\Delta\omega$, it generates what is known as parametric frequency conversion or parametric mode coupling. When one of the modes, e.g., ω_S, is additionally resonantly driven by an external force to amplitude X_S, the parametric mode coupling induces the antisymmetric mode at ω_A to be driven by the combination of X_S and M [cf. Fig. 2(c)] to amplitude X_A. The presence of the spins can thus be inferred from the oscillations, which can be read off at ω_A at either of the two defect locations. In this way, a slow spin inversion can lead to a detectable signal at a high-frequency mode.

III. MODEL DESCRIPTION

We model the system as two equivalent interacting resonators with coordinates x_1 and x_2, corresponding to modes 1 and 2 in Fig. 1. Note that x_1 and x_2 are projections of the full motion of the 2D system onto the normal mode basis [34]. Our treatment is entirely classical, as in our case thermal effects overcome the oscillator's energy level spacing, i.e., $\hbar\omega_0 \ll k_B T$ down to cryogenic temperatures (with $\hbar$ the reduced Planck constant). Mechanical nonlinearities

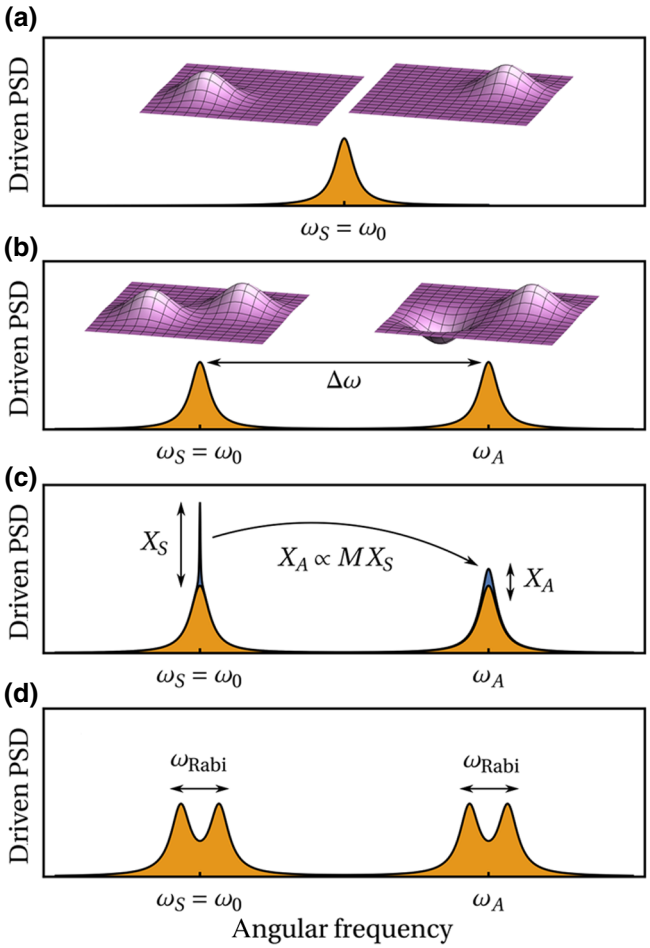

FIG. 2. Mode power spectra at different levels of coupling. (a) The two uncoupled degenerate modes at ω_S. The insets provide schematic representations of the mode shapes. (b) Frequency splitting introduced by linear spatial coupling. (c) Spin-mediated amplitude at ω_A generated by weak parametric modulation and a strong drive at ω_S. (d) Further splitting (Rabi oscillations) due to strong parametric driving (not realized in our case).

are added, as they turn out to play an important role (cf. Sec. V). We designate x_1 to host a time-dependent magnetic moment $\mathbf{M}(t)$ in the presence of an inhomogeneous magnetic field $\mathbf{B}(x_1)$ in the x direction. The goal of our scheme is to measure the magnetization $|\mathbf{M}(t)|$, which corresponds to the net polarization of a nanoscale ensemble of nuclear spins. Additionally, x_2 is externally driven by a force $F(t)$, e.g., by laser radiation pressure. The corresponding Hamiltonian reads

$$H = H_0 + H_1, \tag{2}$$

where H_0 describes two noninteracting nonlinear resonators, and

$$H_1 = \frac{m\omega_0\Delta\omega}{2}(x_1 - x_2)^2 - \mathbf{M}(t)\cdot\mathbf{B}(x_1) - F(t)x_2 \tag{3}$$

contains the linear coupling between the resonators, the field interaction, and the external drive, respectively. The component of spin polarization that is perpendicular to the external field undergoes Larmor precession and does not contribute to the signal. Therefore, $\mathbf{M}(t)\cdot\mathbf{B}(x_1) = M(t)B(x_1)$ and the corresponding equations of motion in the presence of homogeneous dissipation γ are

$$\ddot{x}_1 + \gamma\dot{x}_1 + \omega_0^2[1+\chi_1(t)]x_1 + \omega_0\Delta\omega(x_1 - x_2) + K(x_1) = \frac{1}{m}\left[M(t)\frac{\partial}{\partial x_1}B(x_1) + \xi_1(t)\right] \tag{4}$$

and

$$\ddot{x}_2 + \gamma\dot{x}_2 + \omega_0^2[1+\chi_2(t)]x_2 + \omega_0\Delta\omega(x_2 - x_1) + K(x_2) = \frac{1}{m}[F(t) + \xi_2(t)]. \tag{5}$$

The function $K(x)$ contains all nonlinear elements; cf. Sec. V. The terms $\xi_{1,2}(t)$ and $\chi_{1,2}(t)$ represent thermal and frequency noise, respectively, whose roles are discussed in Sec. VI.

The magnetization $M(t)$ fluctuates with a finite correlation time, known as the spin relaxation time T_1 in NMR experiments. Simultaneously, we apply periodic spin-flipping with frequency Ω, so that

$$M(t) = M\xi_M(t)\cos\Omega t, \tag{6}$$

$$\langle\xi_M(t)\xi_M(t')\rangle = e^{-|t-t'|/T_1}, \tag{7}$$

where $\xi_M(t)$ is a stochastic term with an approximately Lorentzian PSD in the frequency domain. In accord with the frequency mismatch problem discussed above, the spin-flipping rate is slow relative to the membrane mode frequency, $\Omega \ll \omega_0$.

Taking the equilibrium point to be $x_1 = 0$ and expanding $B(x_1)$ yields, to second order [36],

$$\frac{\partial B(x_1)}{\partial x_1} = \left|\frac{\partial B(x_1)}{\partial x_1}\right|_{x_1=0} + \left|\frac{\partial^2 B(x_1)}{\partial x_1^2}\right|_{x_1=0} x_1. \tag{8}$$

Substituting Eq. (8) into Eq. (4), the first derivative of B corresponds to a direct drive of mode 1 by the spin force, which is measured in conventional MRFM by flipping the spin at the resonator frequency, $\Omega = \omega_0$. For $\Omega \ll \omega_0$, this drive is off-resonant and can be neglected. The second term corresponds to a force that is proportional to the amplitude x_1, i.e., it corresponds to a parametric drive [37–39]. This parametric drive is also strongly detuned from the main parametric resonance frequency, which is $\Omega = 2\omega_0$. The frequency shift caused by this term has been observed in experiments [2,7,40,41], but its practical use for nuclear

spin detection is typically hindered by frequency noise in the resonator.

The key role of the higher field derivatives in Eq. (8) is brought out in the normal mode basis (see Fig. 2 for a visualization). Applying the linear transformation

$$\begin{pmatrix} x_S \\ x_A \end{pmatrix} = \frac{1}{\sqrt{2}} \begin{pmatrix} 1 & 1 \\ 1 & -1 \end{pmatrix} \begin{pmatrix} x_1 \\ x_2 \end{pmatrix} \tag{9}$$

yields two normal modes labeled x_S (symmetric) and x_A (antisymmetric), governed by the two equations of motion

$$\begin{aligned} &\ddot{x}_i + \gamma \dot{x}_i + \omega_i^2(t) x_i + K_i(x_i, x_j) \\ &\quad = \delta\omega^2(t) x_j + \frac{F(t)}{\sqrt{2}m} + \frac{\xi_i(t)}{m} \end{aligned} \tag{10}$$

with $i,j \in \{S,A\}$, $i \neq j$. The normal modes are split in frequency [42],

$$\begin{aligned} \omega_S^2(t) &= \omega_0^2 - \delta\omega^2(t), \\ \omega_A^2(t) &= \omega_0^2 + 2\omega_0 \Delta\omega - \delta\omega^2(t), \end{aligned} \tag{11}$$

where

$$\delta\omega^2(t) = \frac{M(t)}{2m} \partial_x^2 B, \tag{12}$$

and from now on we use the shorthand notation $\partial_x^2 B \equiv |\partial^2 B(x_1)/\partial x_1^2|_{x_1=0}$.

The transformed nonlinear terms $K_i(x_i, x_j)$ further couple the two modes. Note that, for resonators with nonidentical frequencies and/or masses, a transformation analogous to Eq. (9) can always be found that cancels the linear coupling term.

IV. LINEAR CASE

Before turning to the key performance characteristic of our proposed scheme—the signal-to-noise ratio (SNR)—in Sec. VI, we demonstrate its working principle on a simple case. To this end, we neglect nonlinearities and noise terms in Eq. (10) and set $T_1 \to \infty$.

It is important to note that $\delta\omega^2(t)$ enters as two different effects. First, it enters Eq. (11) as a (parametric) modulation in time of the normal mode frequencies. As mentioned before, this modulation is far detuned from resonance and can be neglected. Second, $\delta\omega^2(t)$ appears in Eq. (10) as an explicit coupling term between x_S and x_A [35].

Energy up-conversion is equivalent to a driving force exerted by one mode onto the other. Taking, without loss of generality, x_S as the strongly driven "pump" and x_A as the "readout" mode, we set the external force to be $F(t) = F\cos(\omega_S t)$ and write the pump mode amplitude as

$$x_S(t) = X_S \cos(\omega_S t). \tag{13}$$

The oscillating term $\delta\omega^2(t) x_S(t)$ in Eq. (10) now acts as a driving force for x_A that facilitates a frequency conversion: the low-frequency parametric drive $\delta\omega^2(t)$ of the resonator x_1 is up-converted into two driving terms acting on the mode x_A at frequencies $\omega_S \pm \Omega$. Flipping the spins at the modes' frequency difference, $\Omega = \Delta\omega$, hence results in a resonant driving force for x_A with amplitude

$$F_{\text{spin}} = \frac{M \partial_x^2 B}{4} X_S. \tag{14}$$

In this way, the driven pump mode generates a magnetization-dependent motion of the readout mode. We can thus detect M by measuring the Fourier component $\hat{x}_A(\omega_A)$ (denoted X_A), which is proportional to F_{spin} and has a fixed ratio to the pump mode amplitude X_S,

$$X_A = \frac{M \partial_x^2 B}{4 m \omega_A^2} Q X_S, \tag{15}$$

where $Q = \omega_0/\gamma$.

Note that strong parametric coupling of two nondegenerate modes generates doubly split states [see Fig. 2(d)] [43,44]. This can be understood as a periodic redistribution of energy between the modes, akin to Rabi oscillations [35,45,46], which manifest as a beating in the amplitude of each normal mode. The frequency of the Rabi oscillations for a sinusoidal parametric drive $\delta\omega^2(t) \equiv \delta\omega^2 \sin(t\Delta\omega)$ is given by the corresponding natural frequency shift, $\omega_{\text{Rabi}} = \delta\omega^2/2\omega_0$. In our case, however, $\omega_{\text{Rabi}} \ll \gamma \ll \omega_0$, meaning that energy up-converted from ω_S to ω_A is dissipated long before it can be coherently transported back to ω_S. We thus neglect coherent Rabi oscillations and only look for steady-state amplitudes of the normal modes x_S and x_A under the influence of weak energy up-conversion [see Fig. 2(c)].

In summary, we can see that the strong drive at frequency ω_S has been converted into a signal at ω_A that depends linearly on M, i.e., it corresponds to the (instantaneous) magnetization of the measured spin or spin ensemble. Measuring the ratio in Eq. (15), instead of a directly driven resonator amplitude, enables the use of high-frequency resonators as MRFM sensors. Note that, for finite spin lifetimes, this magnetization will turn into a fluctuating quantity whose variance in time represents the signal [29].

V. NONLINEAR EFFECTS

Inspecting Eq. (15) suggests that, in order to maximize the signal amplitude, we should drive the pump mode as

much as possible. However, nonlinearities, which are naturally present in any real system, become non-negligible as the oscillation amplitudes increase. Though such coupled nonlinear equations are difficult to solve, we will see that the effect of nonlinearities on our sensing scheme can be quantified in a straightforward manner.

In line with the contemporary development of defect modes in membrane nanoresonators [34], we consider a combination of a Duffing term α and nonlinear damping terms Γ_1 and Γ_2, such that K in Eqs. (4) and (5) becomes

$$K(x_i) = \frac{\alpha}{m}x_i^3 + (\Gamma_1 x_i^2 + \Gamma_2 \dot{x}_i^2)\dot{x}_i, \qquad i = 1, 2, \tag{16}$$

with our analysis being directly applicable to higher-order nonlinear terms.

Identifying again x_S as the pump mode, we refer to the equations of motion [Eq. (10)] in the limit of $x_S \gg x_A$. The nonlinearity of x_S will shift its resonant frequency and induce motion at higher harmonics of the driving frequency [47]. These higher harmonics generally affect the readout mode x_A nonresonantly, such that the approximation $x_S \approx X_S \cos(\omega_S t)$ remains correct. The readout mode x_A has a much smaller amplitude than x_S because it is not driven resonantly. We can therefore continue to treat it as a linear resonator,

$$\ddot{x}_A + \gamma_A^{\rm nl}(t)\dot{x}_A + \omega_A^{\rm nl}(t)^2 x_A = X_S \delta\omega^2(t)\cos(\omega_S t) + \frac{F(t)}{\sqrt{2}m}. \tag{17}$$

However, nonlinearities in the bare resonators x_1 and x_2 couple the motions of x_S and x_A (cf. Appendix A). The damping term $\gamma_A^{\rm nl}$ and natural frequency $\omega_A^{\rm nl}$ are hence affected by the large amplitude X_S as

$$\begin{aligned}\gamma_A^{\rm nl}(t) &= \gamma + \frac{X_S^2}{4}[\Gamma_1 + 3\omega_S^2\Gamma_2 + (\Gamma_1 - 3\omega_S^2\Gamma_2)\cos(2\omega_S t)],\\ \omega_A^{\rm nl}(t)^2 &= \omega_A^2\{1 + \lambda_1[1 + \cos(2\omega_S t)] + \lambda_2 \sin(2\omega_S t)\},\end{aligned} \tag{18}$$

where

$$\lambda_1 = \frac{3\alpha}{4m\omega_A^2}X_S^2 \quad \text{and} \quad \lambda_2 = \frac{\Gamma_1\omega_S}{2\omega_A^2}X_S^2. \tag{19}$$

The time-dependent terms in Eq. (18) act as off-resonant parametric drives and have no significant effect (cf. Appendix B). Similarly, the natural frequency shift introduced by the Duffing nonlinearity α is negligible ($\lambda_1 \cong 10^{-6}$), precluding significant changes in the response of x_A [48]. Note that λ_1 converts any noise present in the amplitude X_S to frequency noise of x_A [49]. Importantly, though, the effective damping is increased. Defining a nonlinear damping parameter $\Gamma_{\rm nl} = \frac{1}{4}(\Gamma_1 + 3\omega_S^2\Gamma_2)$, the quality factor of the readout mode x_A is lowered to

$$Q_{\rm nl} = \frac{\omega_0}{\gamma + \Gamma_{\rm nl}X_S^2}, \tag{20}$$

which in turn limits the signal gain; cf. Eq. (15) with $Q \to Q_{\rm nl}$. As we show in Sec. VI, the increased damping is also detrimental to the SNR since it increases the thermal noise power, in accordance with the fluctuation-dissipation theorem [cf. Eq. (1)].

VI. STATISTICAL TREATMENT

A. Noise terms in the model

In a realistic setting, the bare resonators [Eqs. (4) and (5)] are subject to both additive thermal white noise $\xi_{1,2}(t)$ and multiplicative frequency noise $\chi_{1,2}(t)$ [50]. In the frequency domain $\xi_{1,2}$ is spectrally flat, whereas $\chi_{1,2}$ will usually drop off as ω^{-1} or ω^{-2} [51]. The observed amplitude of the readout mode x_A is thus a combination of the desired signal and fluctuations in the system. To obtain the SNR, we analyze the additive and multiplicative noise components in Eq. (10) separately.

1. Transformed noise terms

In the normal mode basis, the multiplicative noise is simply

$$\chi_{A,S} = \frac{\chi_1(t) + \chi_2(t)}{2}, \tag{21}$$

while the additive noise has contributions from both additive (thermal) and multiplicative (frequency) noise of the bare oscillators,

$$\xi_{A,S} = \frac{\xi_1(t) \pm \xi_2(t)}{\sqrt{2}} + \frac{m\omega_0^2[\chi_2(t) - \chi_1(t)]}{2}x_{S,A}. \tag{22}$$

Specifically, we note the coherent term x_S entering the additive noise ξ_A; taking x_S to be the monochromatic pump [Eq. (13)], this up-converts the noise from $\chi_1(t)$ and $\chi_2(t)$, creating a qualitatively different noise term in the coupled system.

2. Noise PSD

For equivalent bare oscillators, we assume equal frequency noise PSDs, $S_{\chi_1}(\omega) = S_{\chi_2}(\omega) \equiv S_\chi(\omega)$, whereas the thermal noise PSD is taken constant as per the equipartition theorem, $S_{\xi_1} = S_{\xi_2} \equiv S_\xi$. We then arrive at the PSD

of ξ_A,

$$S_{\xi_A}(\omega) = \frac{2\omega_0 m k_B T}{\pi Q_{\rm nl}} + \frac{(m\omega_0^2 X_S)^2}{8}[S_\chi(\omega-\omega_S) + S_\chi(\omega+\omega_S)], \quad (23)$$

comprising both thermal noise and up-converted frequency noise [52]. The last term in Eq. (23) will typically be negligible due to the fast decay of $S_\chi(\omega)$ with ω.

3. Effect of frequency noise

In general, colored frequency noise is difficult to treat analytically. Exact results have been obtained for dichotomous and trichotomous Markovian noise with a Lorentzian PSD [53–55]. These display a highly complex dependence of the system response on the noise profile, which however only manifests at relatively long coherence times. In our case, the typical noise coherence times τ_c fall within the limit $\gamma \ll \tau_c^{-1} \ll \omega_0$. It has been shown [54] that in this case the noise simply shifts the system slightly off resonance, so that the response [Eq. (15)] decreases to

$$X_A \to X_A\left[1 - \frac{{\rm var}(\omega_A^2)}{\omega_0^4}Q^2\right]. \quad (24)$$

The frequency variance ${\rm var}(\omega_A^2)$ can be obtained via the Wiener-Khinchin theorem by integrating the power spectral density of the dimensionless term $\chi(t)$:

$${\rm var}(\omega_A^2) = \omega_0^4 \int_0^\infty S_\chi(\omega) d\omega. \quad (25)$$

Apart from the intrinsic frequency noise χ, our system is also affected by the conversion of any noise in the pump amplitude X_S into the frequency noise of x_A, as shown in Appendix A. However, both sources result in negligible corrections compared to the effect of thermal noise acting on x_A and we disregard them from now on.

4. Effect of spin fluctuations

We now study the impact of the finite spin lifetime. During the course of a measurement, the magnetization will fluctuate with a characteristic time T_1; cf. Eq. (7). In the frequency domain, this corresponds to a Lorentzian distribution. The signal (i.e., the force PSD due to the nuclear spins) is therefore broadened to give

$$S_{\rm spin}(\omega) = F_{\rm spin}^2 \frac{T_1}{\pi[1+(\omega-\omega_A)^2 T_1^2]}, \quad (26)$$

where $F_{\rm spin}$ is the force originating from parametric driving with a coherent magnetic moment [Eq. (14)]. From a practical perspective (cf. Sec. VII), it is desirable to increase the bandwidth of the resonator beyond the spin lifetime, $2Q/\omega_A < T_1$ [56]. This is routinely achieved by active feedback damping [24,57–59].

5. General displacement PSD

We finally present a formulation of the displacement PSD of the readout mode in the presence of feedback damping and various noise sources. Since we consider the case $k_B T \gg \hbar\omega_A$, we neglect zero-point fluctuations and the discrete nature of the energy spectrum.

We start by defining the susceptibility of the mode as

$$g^2(\omega) = \frac{1/m^2}{(\omega^2-\omega_A^2)^2 + (\omega\omega_A/Q_{\rm fd})^2} \quad (27)$$

with $Q_{\rm fd} = Q_{\rm nl}/(1+p)$ being the (nonlinear) quality factor damped by a feedback gain p. The mode is driven by the fluctuating force $S_{\xi_A}(\omega)$ defined in Eq. (23) and is further subject to detector noise $S_{\rm det}$ and to quantum backaction force noise $S_{\rm qba}$, which represents the non-negligible disturbance of the system by an increasingly precise measurement [57,60]. The latter takes the value

$$S_{\rm qba} = \frac{\hbar^2}{4\pi^2 S_{\rm det}\eta} \quad (28)$$

with $0 < \eta \leq 1$ being the detection efficiency [24]. The observed displacement PSD of the readout mode in the presence of all of these fluctuating forces as well as a spin signal becomes [24,59]

$$S_x(\omega) = g^2(\omega)[S_{\xi_A}(\omega) + S_{\rm qba} + S_{\rm spin}(\omega) + g_{p=0}^{-2}(\omega)S_{\rm det}], \quad (29)$$

where $g_{p=0}^2(\omega)$ is the susceptibility without feedback damping. There are three important points to note here. First, we can see from Eq. (29) that feedback damping decreases the thermomechanical displacement noise PSD, but not the underlying force noise PSD (terms in the bracket on the right-hand side). The benefit of feedback damping for nuclear spin detection is only to allow for rapid sampling of statistically independent spin configurations [56]. Second, the fact that zero-point fluctuations are reduced by feedback damping does not violate the Heisenberg uncertainty principle, since the added measurement uncertainty corresponds to at least one half quantum of energy [24,57]. Third, tuning $S_{\rm det}$, for instance, by varying the laser power in an optical cavity used to detect the resonator motion, enables an optimal measurement that minimizes S_x over a desired bandwidth [60].

6. Filtering

In order to reduce the measured displacement noise, we apply a filter to reject noise far off the signal frequency. As a concrete example, we consider a standard Butterworth filter, which modulates the signal with $G(\omega) = \{1 + [(\omega - \omega_A)/\omega_f]^{2n}\}^{-1/2}$, where ω_f denotes the bandwidth and n the

filter order. The signal of our experiment corresponds to the displacement variance driven by the spin signal,

$$\sigma^2_{\rm spin} = \int_0^\infty G(\omega)^2 g(\omega)^2 S_{\rm spin}(\omega) d\omega, \tag{30}$$

which is measured together with a noise background of

$$\sigma^2_{\rm noise} = \int_0^\infty G(\omega)^2 g(\omega)^2 [S_{\xi_A}(\omega) + S_{\rm qba} + g^{-2}_{p=0}(\omega) S_{\rm det}] d\omega. \tag{31}$$

VII. EXPERIMENT PROPOSAL

We now assess the feasibility of the proposed measurement scheme using representative experimental parameters of patterned Si_3N_4 membranes; cf. Fig. 1. The full set of parameters is included in Appendix E.

First, we need to relate $\sigma^2_{\rm spin}$ to the number of spins in the measured ensemble. To this end, we utilize the MRFM framework of spin variance sensing [56]. For an ensemble of N spins, as N becomes small, the thermal (Boltzmann) polarization scales as N and is eventually outweighed by the spin noise, whose standard deviation scales as $\sqrt{N}$. The preferred measurable quantity at the nanoscale is hence the magnetization variance

$$\langle M^2 - \langle M \rangle^2 \rangle = N\mu^2, \tag{32}$$

where $\mu = 1.4 \times 10^{-26}\,{\rm J\,T^{-1}}$ is the proton magnetic moment. Assuming that $\langle M \rangle \cong 0$, the expected spin force is then $\langle F^2_{\rm spin} \rangle \propto N\mu^2$. Our aim is to estimate the variance by taking successive noisy readings of M as it fluctuates in time, and hence determine N. For a spin ensemble with lifetime T_1 and matched filter bandwidth $\omega_f = 1/T_1$, in the limits $\sigma^2_{\rm spin} \ll \sigma^2_{\rm noise}$, we can represent the SNR after a collection time $t_c \gg T_1$ in the concise form [56]

$$s_{\rm SNR} = \frac{1}{2}\sqrt{\frac{t_c}{T_1}}\frac{\sigma^2_{\rm spin}}{\sigma^2_{\rm noise}}. \tag{33}$$

Equation (33) is the most important characteristic of the proposed experiment.

A. Expected SNR

Let us now evaluate the SNR of the feedback-damped system [Eq. (33)]. Driving the pump mode X_S stronger boosts the SNR via the parametric conversion into the force $|F_{\rm spin}|$ [cf. Eqs. (14) and (26)]. However, it also increases the readout mode dissipation via nonlinear damping [Eq. (20)], which in turn increases thermal fluctuations [Eq. (23)].

1. Asymptotic limit

The nonlinear damping eventually becomes the dominant dissipation mechanism, whereby, for

$$\Gamma_{\rm nl} \gg \gamma / X_S^2, \tag{34}$$

both the signal and the thermal noise PSD scale as X_S^2, resulting in a limiting value of the SNR,

$$\lim_{X_S \to \infty} s_{\rm SNR} = \frac{C_n (\mu \partial_x^2 B)^2}{64 k_B T m \Gamma_{\rm nl}} N \sqrt{t_c T_1}, \tag{35}$$

where

$$C_n = \frac{\int_0^\infty [(1+z^{2n})(1+z^2)]^{-1} dz}{\int_0^\infty (1+z^{2n})^{-1} dz} \tag{36}$$

is a dimensionless constant, depending solely on the filter order n. Note that Eq. (35) is independent of the intrinsic linear damping parameter γ, assuming that it is possible to drive the system strongly enough to satisfy the inequality in Eq. (34).

2. Case study

We proceed to calculate the expected SNR [Eq. (33)] for values motivated by recent experiments [24]. The filtering constant C_n [Eq. (36)] increases with n; we use the value $n = 4$ ($C_4 \cong 0.77$) as higher orders bring negligible improvement. A plot of the SNR against the pump mode amplitude for three representative values of $\Gamma_{\rm nl}$ is shown in Fig. 3. All parameters are taken from Appendix E unless stated otherwise.

The current membrane devices typically possess $\Gamma_{\rm nl} \cong 1 \times 10^{14}\,{\rm m^{-2}\,s^{-1}}$ [34]. In Fig. 3, we see that this allows a SNR exceeding 1 at relatively modest pump mode amplitudes of $X_S = 10$ nm and collection times of 240 s, approaching 9.5 at stronger pumping. [Please note that the spatially resolved amplitudes of $x_{1,2}$ are equal to $X_S/\sqrt{2}$; cf. Eq. (9). For $X_S = 10$ nm, the spin sample therefore moves with an amplitude of 7.1 nm.] This projected performance is on par with current state-of-the-art MRFM experiments, although with a significant potential for improvement stemming from the unusual sensing mechanism (cf. Sec. VII B).

A breakdown of the different noise sources in terms of their impact on the observed displacement is shown in Fig. 4. The principal noise component is the thermomechanical noise.

B. Discussion and conclusions

The SNR results presented in Fig. 3 compare favorably to recent MRFM experiments. We expect to reach a SNR value of 1 after 240 seconds of measurement with ensemble sizes around $N \sim 10^4$ spins, which matches

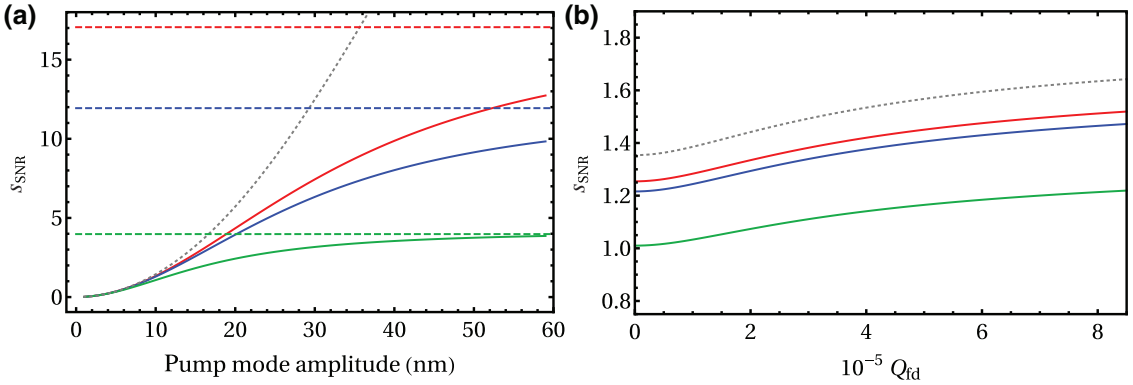

FIG. 3. The SNR [cf. Eq. (33)] as a function of (a) pump mode amplitude X_S and (b) feedback-damped quality factor Q_{fd}. The lines correspond to nonlinear damping values $\Gamma_{\mathrm{nl}} = 7 \times 10^{13}\,\mathrm{m}^{-2}\,\mathrm{s}^{-1}$ (red solid line), $1 \times 10^{14}\,\mathrm{m}^{-2}\,\mathrm{s}^{-1}$ (blue solid line), $3 \times 10^{14}\,\mathrm{m}^{-2}\,\mathrm{s}^{-1}$ (green solid line) and no nonlinear damping (gray dotted line). The collection time is $t_c = 240$ s and we consider an ensemble size of 10^4 proton spins at $T = 0.2$ K, as well as $T_1 = 50$ ms, and $S_{\mathrm{det}} = 10^{-31}\,\mathrm{m}^2\,\mathrm{s}$ (cf. other values given in Appendix E). In (a), the quality factor is $Q_{\mathrm{fd}} = 2 \times 10^5$, and the dashed lines show the respective asymptotic limits [cf. Eq. (35)]. In (b), the pump mode amplitude is 10 nm.

the sensitivity of current state-of-the-art measurements obtained with ultrasoft cantilevers and nanowires [10,11,29]. Further significant improvements are expected since the design of ultracoherent nanoscale resonators is an area of active research. As shown in Eq. (35), the instrumental limitation to the SNR depends on the product $(m\Gamma_{\mathrm{nl}})^{-1}$. On the one hand, low mass m can readily be achieved by designing thin ribbons instead of a drum-mode resonator. On the other hand, the nonlinear damping coefficient Γ_{nl} has hitherto not received much attention. Optimizing the resonator design accordingly could open up unprecedented sensitivities in nuclear spin sensing.

Our scheme offers significant practical advantages over instruments based on cantilevers or nanowires. (i) The membrane surface is convenient for placement of "large" samples, such as viruses or biological molecules in the 100 nm range. (ii) The spring constant of the membrane resonator modes is orders of magnitude higher than that of typical MRFM cantilevers, which results in a drastically reduced susceptibility towards spatially varying interaction potentials that affect the sensitivity. The scheme is easily extendable to oscillators with unequal masses and natural frequencies. (iii) Our parametric up-conversion scheme does not require any electrical or magnetic signal at the frequency of the detection mode. This will be helpful to avoid spurious driving of the sensor, which can make data interpretation difficult. (iv) Finally, the magnetic field gradient source in our scheme is located on the scanning tip, which allows us to utilize commercial magnetic force microscopy (MFM) probes. Membrane-based

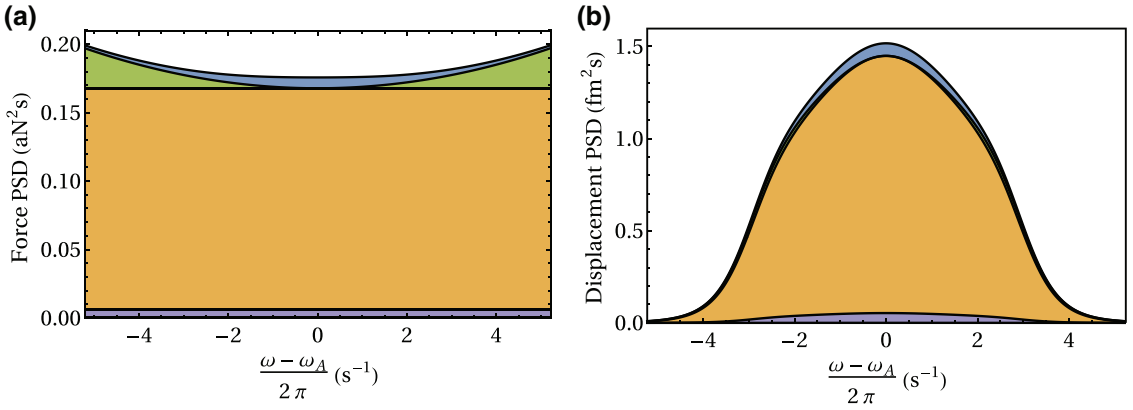

FIG. 4. A cumulative plot of (a) the force PSD [36] acting on the readout mode [cf. Eq. (29)] and (b) the resulting filtered displacement PSD [cf. Eq. (31)]. The individual contributions correspond to the quantum backaction [purple region; cf. Eq. (28)], effective thermal noise S_{ξ_A} (orange region), detector noise S_{det} (green region), and the spin signal S_{spin} [blue region; cf. Eq. (26)]. We use conservative values for $S_{\mathrm{det}} = 10^{-31}\,\mathrm{m}^2\,\mathrm{s}$, and $T = 0.2$ K, $T_1 = 50$ ms, $Q_{\mathrm{fd}} = 2 \times 10^5$, $\Gamma_{\mathrm{nl}} = 1 \times 10^{14}\,\mathrm{m}^{-2}\,\mathrm{s}^{-1}$, $X_S = 10$ nm. (Other values are given in Appendix E.)

MRFM thus has the potential to become a mature and versatile nano-MRI platform.

In summary, we theoretically demonstrate the feasibility of using megahertz optomechanical membrane resonators as force sensors for nuclear spins. Our work highlights the potential of membrane platforms for sensitive spin detection and should encourage further development of membrane-based nano-MRI instruments and spin-mechanics quantum information platforms.

ACKNOWLEDGMENTS

For fruitful discussions and inspiration, we acknowledge A. Schliesser, Y. Tsaturyan, and L. Catalini. This work was supported by the Swiss National Science Foundation through grant CRSII5 177198/1, PP00P2_163818.

APPENDIX A: THE EFFECT OF NONLINEARITIES ON NORMAL MODES

The transformation in Eq. (9) can be applied to the nonlinear equation of motion, although this no longer decouples x_S and x_A. Taking the difference $x_1 - x_2$ from Eqs. (4) and (5), we obtain, after rearranging and leaving out the noise terms,

$$\ddot{x}_A + \left[\gamma + \frac{\Gamma_1}{2}(x_S^2 + x_A^2) + \frac{\Gamma_2}{2}(3\dot{x}_S^2 + \dot{x}_A^2)\right]\dot{x}_A + \left[\omega_0^2 + 2\omega_0\Delta\omega + \frac{\alpha}{2m}x_A^2 + \frac{3\alpha}{2m}x_S^2 + \Gamma_1 x_S\dot{x}_S\right]x_A = \frac{M(t)\partial_x^2 B}{2m}(x_S + x_A) + \frac{F(t)}{\sqrt{2}m}. \tag{A1}$$

Since $x_S \gg x_A$, we can drop all higher-order x_A terms in Eq. (A1). The readout mode thus behaves as a linear oscillator, but with an x_S-dependent damping and spring constant. Nonlinearity of the mode x_S itself plays no role in the detection mechanism; we can thus continue to write its amplitude as $x_S = X_S\cos(\omega_S t)$. Equation (A1) hence simplifies to the form used in Sec. V.

We note that, in general, the pump mode x_S is subject to thermal noise. Looking at the prefactor of x_A in Eq. (A1), we see that this is converted to frequency noise of x_A via the Duffing nonlinearity α [49,61,62]. Let us describe the noisy pump by $X_S = (X_{S0} + \delta X_S)\cos(\omega_S t)$, where the δX_S is the stochastic contribution of thermal noise. To leading order, this affects the frequency of x_A,

$$\omega_A^2 = \omega_0^2 + 2\omega_0\Delta\omega + \frac{3\alpha}{m}X_{S0}\delta X_S\cos^2(\omega_S t). \tag{A2}$$

Taking $\langle\delta X_S\rangle = 0$ and $\langle\delta X_S^2\rangle = k_B T/m\omega_S^2$ and dropping the oscillatory off-resonant terms, this introduces a variance of the frequency ω_A^2,

$$\mathrm{var}(\omega_A^2) = \frac{3}{8}\left(\frac{3\alpha}{m}\right)^2 X_{S0}^2\langle\delta X_S^2\rangle. \tag{A3}$$

For the reference values in Appendix E and $X_{S0} = 10$ nm, we obtain $\mathrm{var}(\omega_A^2) = 1.4\times10^7\ \mathrm{s}^{-4}$. While this is far higher than the intrinsic frequency noise, it does not significantly diminish the resonant response of x_A [cf. Eq. (24)].

APPENDIX B: SPURIOUS PARAMETRIC TERMS IN THE NONLINEAR REGIME

Exciting the pump mode imparts multiple parametric drives on the readout mode; cf. Eqs. (18) and (19). The effect of parametric driving is well explored in the resonant case, where the spring constant is varied at twice the resonator's natural frequency [63]. The response amplitude in that case increases or decreases depending on the relative phase of the parametric and external drives, a phenomenon known as parametric squeezing [38].

In Eq. (18), however, the spurious parametric terms oscillate at $2\omega_S$ and are thus strongly detuned from $2\omega_A$. A straightforward perturbative treatment then shows that the drive induces spurious motion at frequencies $|\omega_A \pm 2\omega_S|$. The signal, extracted from the Fourier component at ω_A, is therefore unaffected. The result calculated earlier for the linear regime remains valid even in the presence of nonlinearities, with Q replaced by Q_{nl}. It is in principle possible for the drives to cause parametric instabilities; however, as our prospective system is far from the unstable regime, we do not pursue this issue further.

APPENDIX C: MAGNETIC FIELD SIMULATIONS

The magnetic field profile is estimated by modeling a hollow conical tip with a rounded top [cf. Fig. 5(a)] with the magnetostatics package RADIA [64]. The tip is assumed to be magnetized to 1.83 T parallel to the x axis [29]. A plot of the spatial profile of the second field gradient $\partial^2 B_x/\partial x^2$ is shown in Fig. 5(b). At 50 nm above the tip center, we obtain $\partial^2 B_x/\partial x^2 = 2\times10^{14}\,\mathrm{T\,m^{-2}}$.

In a MRFM experiment, the spin-containing voxels constituting the sample cannot be scanned individually in real space. Instead, the frequency ω_{rf} of the rf spin-flipping field is swept from $\omega_{\mathrm{rf},0} - \Delta\omega_{\mathrm{rf}}$ to $\omega_{\mathrm{rf},0} + \Delta\omega_{\mathrm{rf}}$. Spins whose Larmor frequency lies within these bounds are flipped, producing a signal proportional to the second field gradient; cf. Sec. III. The signal magnitude due to a spin at position $\mathbf{r}$ is hence a function of space, known as the point spread function (PSF). Here, we define the PSF as

$$\mathrm{PSF}(\mathbf{r}) = \left[\frac{\partial^2 B_x(\mathbf{r})}{\partial x^2}\right]^2\left[1 - \left(\frac{\gamma_n|\mathbf{B}(\mathbf{r})| - \omega_{\mathrm{rf},0}}{\Delta\omega_{\mathrm{rf}}}\right)^2\right] \tag{C1}$$

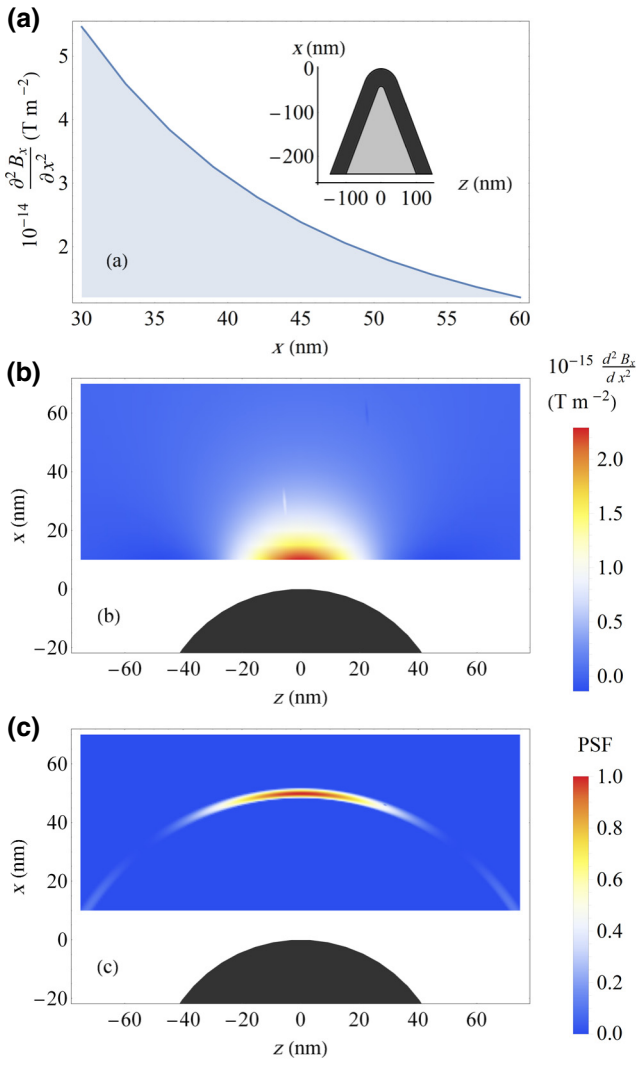

FIG. 5. Magnetic field modeling results. (a) The second field gradient along the central axis of the magnetic tip; (inset) cross section of the tip model, consisting of a nonmagnetic conical base (light gray region) and a layer of magnetic material (dark gray region); (b) simulated second field gradient in the central plane of symmetry; (c) simulated PSF [cf. Eq. (C1)], normalized to the value at 50 nm above the tip center. We used $\Delta\omega_{\rm rf}/\gamma_n = 10$ mT.

for $\gamma_n|\mathbf{B}(\mathbf{r}) - B_0| \leq \Delta\omega_{\rm rf}$ and 0 otherwise, with γ_n being the nuclear spin gyromagnetic ratio. The bracketed term is an empirical expression describing flipping fidelity, whereby spins further off the central resonant condition produce less signal [2].

We plot the PSF in Fig. 5(c), using for $\omega_{\rm rf,0}$ the Larmor frequency 50 nm above the tip center. Note that in conventional MRFM, where the transducer is a cantilever moving along the z axis, the relevant gradient would be $\partial B_x/\partial z$, which results in PSF maxima near the edges of the tip [2]. With our proposed method based on $\partial B_x/\partial x$, these maxima persist but cannot be used due to the vertical motion of the membrane. We however find an additional active area on the central axis of the magnetic tip that makes for a feasible sample position.

APPENDIX D: SPIN DYNAMICS ON THE MOVING MEMBRANE

A conceivable drawback of our scheme is the impact of the high pump mode amplitude, as well as the thermal motion of the membrane, on the spin ensemble. Since the ensemble moves rapidly through a region with a field gradient, its lifetime may be decreased by undergoing nonadiabatic dynamics. In particular, the effect of thermal noise has previously been found to be important in the context of cantilever-based MRFM [65,66].

We describe the flipping in the frame rotating with the Larmor frequency about the x axis, where, under the effect of an applied rf field $B_{\rm rf}(t)\cos[\omega_{\rm rf}(t)]\hat{\mathbf{e}}_z$, the effective field reads

$$\mathbf{B}_{\rm rf}(t) = \begin{pmatrix} \omega_{\rm rf}(t)/\gamma_n \\ 0 \\ B_{\rm rf}(t) \end{pmatrix} \tag{D1}$$

with the spin dynamics being governed by the Bloch equation,

$$\dot{\mathbf{M}}(t) = \gamma_n \mathbf{M}(t) \times \mathbf{B}_{\rm rf}(t). \tag{D2}$$

Starting with $\mathbf{B}_{\rm rf}(t)$ parallel to the x axis, a spin-flip is achieved by an adiabatic sweep across the Larmor frequency. For simplicity, we take a sinusoidal rf profile,

$$\mathbf{B}_{\rm rf}(t) = B_{\rm rf} \begin{pmatrix} \cos(\Delta\omega t) \\ 0 \\ \sin(\Delta\omega t) \end{pmatrix} \tag{D3}$$

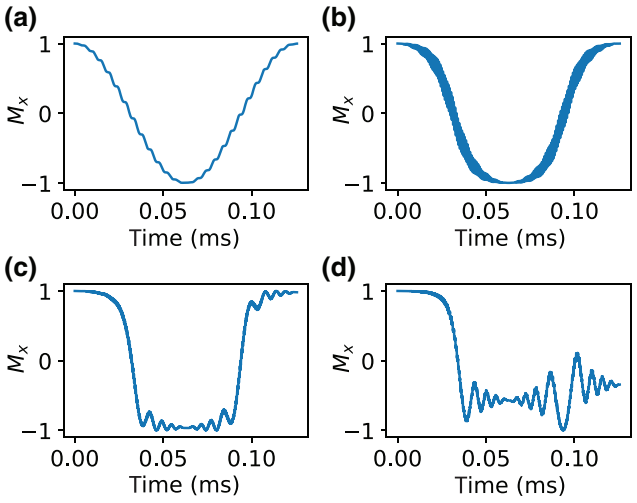

FIG. 6. Magnetization component along the x axis in the flipping process under increasing values of the pump amplitude: (a) $X_S = 0$, (b) $X_S = 10$ nm, (c) $X_S = 50$ nm, (d) $X_S = 100$ nm.

TABLE I. Reference resonator parameters and magnetic field characteristics.

m (ng)	1	Resonator mass
ω_0 (s^{-1})	8.2×10^6	Resonator natural frequency
Q	10^8	Quality factor
α (kg m^{-2} s^{-2})	1×10^{12}	Coefficient of Duffing nonlinearity
$\omega_A - \omega_S$ (s^{-1})	5×10^4	Normal mode frequency splitting
var(x_1) (m^2)	2.2×10^{-20}	Thermal displacement variance at room temperature
$\partial_x B$ (T m^{-1})	6×10^6	Magnetic field gradient $\partial B_x/\partial x$
$\partial_x^2 B$ (T m^{-2})	2×10^{14}	Second magnetic field gradient $\partial^2 B_x/\partial x^2$
η	0.5	Detection efficiency
$S_{\rm det}$ (m^2 s)	10^{-31}	Detector noise PSD
var(ω_A^2) (s^{-4})	10^{-1}	Frequency variance due to intrinsic frequency noise
$S_\chi(\omega_A - \omega_S)$ (s^{-1})	$\leq 10^{-36}$	Relative intrinsic frequency noise PSD at resonance

with $B_{\rm rf} = 5$ mT [29] and $\Delta\omega = \omega_A - \omega_S = 5 \times 10^4$ s^{-1}. Optimizing the pulse profiles will likely provide even more stable spin inversions [29].

1. Motion of the pump mode

When the pump mode oscillates with amplitude X_S [cf. Eqs. (9) and (13)], the sample position is $x_1(t) = X_S \cos(\omega_S t)/\sqrt{2}$. Such a motion is equivalent to a spurious time-dependent field

$$\delta\mathbf{B}(t) = \frac{X_S}{\sqrt{2}} \frac{\partial B_x}{\partial x} \cos(\omega_S t)\hat{\mathbf{e}}_x. \tag{D4}$$

We solve Eq. (D2) numerically with the field $\mathbf{B}_{\rm rf}(t) + \delta\mathbf{B}(t)$. From the field modeling in Appendix C, we obtain $\partial B_x/\partial x = 6 \times 10^6$ T m^{-1}.

In Fig. 6 we show the flipping process under increasing values of X_S. We observe that the spurious field induces oscillatory features in the flipping process, but only causes significant distortion at very strong ($X_S \approx 100$ nm) pumping.

Finally, to test the flipping fidelity, we integrated Eq. (D2) over 250 flips using $X_S = 10$ nm. Starting with a unit vector $\mathbf{M}(0) = \hat{\mathbf{e}}_x$, the magnetization M_x at the end of each flip never dropped below 0.996. We thus conclude that the flipping mechanism remains robust under strong driving of the pump mode.

2. Thermal noise in the membrane

We measured the thermal displacement on one of the defect mode sites of a Si_3N_4 membrane. At room temperature, a root-mean-square displacement of 150 pm is observed, most of which is due to the many delocalized modes of the membrane. Since cantilever-based MRFM displays high flipping fidelities at comparable displacement noise levels, and since our envisioned operational temperature (0.2 K) will further reduce thermal fluctuations, we do not expect this to be an issue with regards to spin-flipping.

APPENDIX E: REFERENCE VALUES

All resonator parameters used in Sec. VII are shown in Table I. The values are taken from recent experimental data [34]. Note that a different, nonunitary normal mode transformation is typically used in the experimental literature:

$$\begin{pmatrix} x_S \\ x_A \end{pmatrix} = \begin{pmatrix} 1 & 1 \\ 1 & -1 \end{pmatrix} \begin{pmatrix} x_1 \\ x_2 \end{pmatrix}. \tag{E1}$$

Relative to our notation, this scales the cubic nonlinearities $\alpha, \Gamma_{\rm nl}$ by a factor of $\frac{1}{2}$ and the mass m by a factor of 2. This transformation is convenient for experimental use, but requires additional renormalization when dealing with external forces.

The magnetic field gradients are estimated by modeling a conical magnetic tip made of saturated Nd-Fe-B magnet (such as is used in MFM) with the magnetostatics package RADIA [64]. The sample is assumed to be positioned directly above the center of the magnetic tip, where there is a relatively large area of constant $\partial_x^2 B$.

[1] J. A. Sidles, Noninductive detection of single-proton magnetic resonance, Appl. Phys. Lett. **58**, 2854 (1991).
[2] C. L. Degen, M. Poggio, H. J. Mamin, C. T. Rettner, and D. Rugar, Nanoscale magnetic resonance imaging, Proc. Natl. Acad. Sci. USA **106**, 1313 (2009).
[3] M. Poggio and C. L. Degen, Force-detected nuclear magnetic resonance: Recent advances and future challenges, Nanotechnology **21**, 342001 (2010).
[4] H. J. Mamin, M. Kim, M. H. Sherwood, C. T. Rettner, K. Ohno, D. D. Awschalom, and D. Rugar, Nanoscale nuclear magnetic resonance with a nitrogen-vacancy spin sensor, Science **339**, 557 (2013).
[5] T. Staudacher, F. Shi, S. Pezzagna, J. Meijer, J. Du, C. A. Meriles, F. Reinhard, and J. Wrachtrup, Nuclear magnetic resonance spectroscopy on a (5-nanometer)^3 sample, Science **339**, 561 (2013).
[6] M. Loretz, S. Pezzagna, J. Meijer, and C. L. Degen, Nanoscale nuclear magnetic resonance with a 1.9-nm-deep

nitrogen-vacancy sensor, Appl. Phys. Lett. **104**, 033102 (2014).
[7] D. Rugar, R. Budakian, H. J. Mamin, and B. W. Chui, Single spin detection by magnetic resonance force microscopy, Nature **430**, 329 (2004).
[8] J. M. Nichol, E. R. Hemesath, L. J. Lauhon, and R. Budakian, Nanomechanical detection of nuclear magnetic resonance using a silicon nanowire oscillator, Phys. Rev. B **85**, 054414 (2012).
[9] J. M. Nichol, T. R. Naibert, E. R. Hemesath, L. J. Lauhon, and R. Budakian, Nanoscale Fourier-Transform Magnetic Resonance Imaging, Phys. Rev. X **3**, 031016 (2013).
[10] B. A. Moores, A. Eichler, Y. Tao, H. Takahashi, P. Navaretti, and C. L. Degen, Accelerated nanoscale magnetic resonance imaging through phase multiplexing, Appl. Phys. Lett. **106**, 213101 (2015).
[11] W. Rose, H. Haas, A. Q. Chen, N. Jeon, L. J. Lauhon, D. G. Cory, and R. Budakian, High-Resolution Nanoscale Solid-State Nuclear Magnetic Resonance Spectroscopy, Phys. Rev. X **8**, 011030 (2018).
[12] H. J. Mamin and D. Rugar, Sub-attonewton force detection at millikelvin temperatures, Appl. Phys. Lett. **79**, 3358 (2001).
[13] J. Moser, J. Güttinger, A. Eichler, M. J. Esplandiu, D. E. Liu, M. I. Dykman, and A. Bachtold, Ultrasensitive force detection with a nanotube mechanical resonator, Nat. Nanotechnol. **8**, 493 (2013).
[14] Y. Tao, J. M. Boss, B. A. Moores, and C. L. Degen, Single crystal diamond nanomechanical resonators with quality factors exceeding one million, Nat. Commun. **5**, 3638 (2014).
[15] P. Weber, J. Güttinger, A. Noury, J. Vergara-Cruz, and A. Bachtold, Force sensitivity of multilayer grapheneoptomechanical devices, Nat. Commun. **7**, 12496 (2016).
[16] C. Reinhardt, T. Müller, A. Bourassa, and J. C. Sankey, Ultralow-Noise sin Trampoline Resonators for Sensing and Optomechanics, Phys. Rev. X **6**, 021001 (2016).
[17] R. A. Norte, J. P. Moura, and S. Gröblacher, Mechanical Resonators for Quantum Optomechanics Experiments at Room Temperature, Phys. Rev. Lett. **116**, 147202 (2016).
[18] N. Rossi, F. R. Braakman, D. Cadeddu, D. Vasyukov, G. Tutuncuoglu, A. F. i Morral, and M. Poggio, Vectorial scanning force microscopy using a nanowire sensor, Nat. Nanotechnol. **12**, 150 (2017).
[19] L. M. de Lepinay, B. Pigeau, B. Besga, P. Vincent, P. Poncharal, and O. Arcizet, A universal and ultrasensitive vectorial nanomechanical sensor for imaging 2D force fields, Nat. Nanotechnol. **12**, 156 (2017).
[20] Y. Tsaturyan, A. Barg, E. S. Polzik, and A. Schliesser, Ultracoherent nanomechanical resonators via soft clamping and dissipation dilution, Nat. Nanotechnol. **12**, 776 (2017).
[21] M. Heritier, A. Eichler, Y. Pan, U. Grob, I. Shorubalko, M. D. Krass, Y. Tao, and C. L. Degen, Nanoladder cantilevers made from diamond and silicon, Nano Lett. **18**, 1814 (2018).
[22] S. L. de Bonis, C. Urgell, W. Yang, C. Samanta, A. Noury, J. Vergara-Cruz, Q. Dong, Y. Jin, and A. Bachtold, Ultrasensitive displacement noise measurement of carbon nanotube mechanical resonators, Nano Lett. **18**, 5324 (2018).
[23] A. H. Ghadimi, S. A. Fedorov, N. J. Engelsen, M. J. Bereyhi, R. Schilling, D. J. Wilson, and T. J. Kippenberg, Elastic strain engineering for ultralow mechanical dissipation, Science **360**, 764 (2018).
[24] M. Rossi, D. Mason, J. Chen, Y. Tsaturyan, and A. Schliesser, Measurement-based quantum control of mechanical motion, Nature **563**, 53 (2018).
[25] N. Scozzaro, W. Ruchotzke, A. Belding, J. Cardellino, E. Blomberg, B. McCullian, V. Bhallamudi, D. Pelekhov, and P. Hammel, Magnetic resonance force detection using a membrane resonator, J. Magn. Reson. **271**, 15 (2016).
[26] M. Blankenhorn, E. Heintze, M. Slota, J. van Slageren, B. A. Moores, C. L. Degen, L. Bogani, and M. Dressel, Membrane-based torque magnetometer: Enhanced sensitivity by optical readout of the membrane displacement, Rev. Sci. Instrum. **88**, 094707 (2017).
[27] H. Takahashi, T. Okamoto, K. Ishimura, S. Hara, E. Ohmichi, and H. Ohta, Force-detected high-frequency electron spin resonance spectroscopy using magnet-mounted nanomembrane: Robust detection of thermal magnetization modulation, Rev. Sci. Instrum. **89**, 083905 (2018).
[28] R. Fischer, D. P. McNally, C. Reetz, G. G. T. Assumpção, T. Knief, Y. Lin, and C. A. Regal, Spin detection with a micromechanical trampoline: Towards magnetic resonance microscopy harnessing cavity optomechanics, New J. Phys. **21**, 043049 (2019).
[29] U. Grob, M.-D. Krass, M. Héritier, R. Pachlatko, J. Rhensius, J. Košata, B. A. J. Moores, H. Takahashi, A. Eichler, and C. L. Degen, Magnetic resonance force microscopy with a one-dimensional resolution of 0.9 nanometers, Nano Lett. **19**, 7935 (2019).
[30] W. M. Dougherty, K. J. Bruland, J. L. Garbini, and J. A. Sidles, Detection of ac magnetic signals by parametric mode coupling in a mechanical oscillator, Meas. Sci. Technol. **7**, 1733 (1996).
[31] E. W. Moore, S. Lee, S. A. Hickman, L. E. Harrell, and J. A. Marohn, Evading surface and detector frequency noise in harmonic oscillator measurements of force gradients, Appl. Phys. Lett. **97**, 044105 (2010).
[32] M. Aspelmeyer, T. J. Kippenberg, and F. Marquardt, Cavity optomechanics, Rev. Mod. Phys. **86**, 1391 (2014).
[33] M. de Wit, G. Welker, J. J. T. Wagenaar, F. G. Hoekstra, and T. H. Oosterkamp, Feasibility of imaging in nuclear magnetic resonance force microscopy using boltzmann polarization, J. Appl. Phys. **125**, 083901 (2019).
[34] L. Catalini, Y. Tsaturyan, and A. Schliesser, Soft-Clamped Phononic Dimers for Mechanical Sensing and Transduction, Phys. Rev. Appl. **14**, 014041 (2020).
[35] M. Frimmer and L. Novotny, The classical bloch equations, Am. J. Phys **82**, 947 (2014).
[36] Note that higher order terms introduce nonlinearities into the equation of motion, but here these are negligible in magnitude.
[37] D. Rugar and P. Grütter, Mechanical Parametric Amplification and Thermomechanical Noise Squeezing, Phys. Rev. Lett. **67**, 699 (1991).
[38] R. Lifshitz and M. C. Cross, in *Reviews of Nonlinear Dynamics and Complexity*, edited by H. G. Schuster (Wiley-VCH Verlag GmbH & Co. KGaA, Weinheim, 2008).

[39] A. Leuch, L. Papariello, O. Zilberberg, C. L. Degen, R. Chitra, and A. Eichler, Parametric Symmetry Breaking in a Nonlinear Resonator, Phys. Rev. Lett. **117**, 214101 (2016).

[40] S. R. Garner, S. Kuehn, J. M. Dawlaty, N. E. Jenkins, and J. A. Marohn, Force-gradient detected nuclear magnetic resonance, Appl. Phys. Lett. **84**, 5091 (2004).

[41] S. G. Lee, E. W. Moore, and J. A. Marohn, Unified picture of cantilever frequency shift measurements of magnetic resonance, Phys. Rev. B **85**, 165447 (2012).

[42] Please note that the elastic coupling energy term proportional to $(x_1 - x_2)^2$ does not affect the symmetric mode while it raises the frequency of the antisymmetric mode. The more common situation where the coupling is proportional to $x_1 x_2$ (e.g., Rabi splitting) results in a symmetric splitting around ω_0.

[43] H. Okamoto, A. Gourgout, C.-Y. Chang, K. Onomitsu, I. Mahboob, E. Y. Chang, and H. Yamaguchi, Coherent phonon manipulation in coupled mechanical resonators, Nat. Phys. **9**, 480 (2013).

[44] B. Abdo, A. Kamal, and M. Devoret, Nondegenerate three-wave mixing with the josephson ring modulator, Phys. Rev. B **87**, 014508 (2013).

[45] T. Faust, J. Rieger, M. J. Seitner, J. P. Kotthaus, and E. M. Weig, Coherent control of a classical nanomechanical two-level system, Nat. Phys. **9**, 485 (2013).

[46] H. Okamoto, A. Gourgout, C.-Y. Chang, K. Onomitsu, I. Mahboob, E. Y. Chang, and H. Yamaguchi, Coherent phonon manipulation in coupled mechanical resonators, Nat. Phys. **9**, 480 (2013).

[47] R. H. Rand, *Lecture Notes on Nonlinear Vibration* (Internet-First University Press, Ithaca, 2005). http://audiophile.tam.cornell.edu/randdocs/nlvibe52.pdf.

[48] R. Lifshitz and M. Cross, Response of parametrically driven nonlinear coupled oscillators with application to micromechanical and nanomechanical resonator arrays, Phys. Rev. B **67**, 134302 (2003).

[49] E. Kenig, M. Cross, L. Villanueva, R. Karabalin, M. Matheny, R. Lifshitz, and M. Roukes, Optimal operating points of oscillators using nonlinear resonators, Phys. Rev. E **86**, 056207 (2012).

[50] A. Cleland and M. Roukes, Noise processes in nanomechanical resonators, J. Appl. Phys. **92**, 2758 (2002).

[51] K. Y. Fong, W. H. P. Pernice, and H. X. Tang, Frequency and phase noise of ultrahigh q silicon nitride nanomechanical resonators, Phys. Rev. B **85**, 161410 (2012).

[52] Note that as we are using a single-sided PSD as a function of angular frequency ω, the thermal noise appears with a factor of $2/\pi$ instead of the more familiar case of a PSD as a function of frequency $f = \omega/2\pi$, which results in a factor 4.

[53] R. Bourret, U. Frisch, and A. Pouquet, Brownian motion of harmonic oscillator with stochastic frequency, Physica **65**, 303 (1973).

[54] M. Gitterman, Harmonic oscillator with multiplicative noise: Nonmonotonic dependence on the strength and the rate of dichotomous noise, Phys. Rev. E **67**, 057103 (2003).

[55] R. Mankin, K. Laas, T. Laas, and E. Reiter, Stochastic multiresonance and correlation-time-controlled stability for a harmonic oscillator with fluctuating frequency, Phys. Rev. E **78**, 031120 (2008).

[56] C. L. Degen, M. Poggio, H. J. Mamin, and D. Rugar, Role of Spin Noise in the Detection of Nanoscale Ensembles of Nuclear Spins, Phys. Rev. Lett. **99**, 250601 (2007).

[57] J.-M. Courty, A. Heidmann, and M. Pinard, Quantum limits of cold damping with optomechanical coupling, Eur. Phys. J. D **17**, 399 (2001).

[58] D. Kleckner and D. Bouwmeester, Sub-kelvin optical cooling of a micromechanical resonator, Nature **444**, 75 (2006).

[59] M. Poggio, C. L. Degen, H. J. Mamin, and D. Rugar, Feedback Cooling of a Cantilever's Fundamental Mode below 5 mk, Phys. Rev. Lett. **99**, 017201 (2007).

[60] A. A. Clerk, M. H. Devoret, S. M. Girvin, F. Marquardt, and R. J. Schoelkopf, Introduction to quantum noise, measurement, and amplification, Rev. Mod. Phys. **82**, 1155 (2010).

[61] L. Villanueva, E. Kenig, R. Karabalin, M. Matheny, R. Lifshitz, M. Cross, and M. Roukes, Surpassing Fundamental Limits of Oscillators Using Nonlinear Resonators, Phys. Rev. Lett. **110**, 177208 (2013).

[62] B. Yurke, D. Greywall, A. Pargellis, and P. Busch, Theory of amplifier-noise evasion in an oscillator employing a nonlinear resonator, Phys. Rev. A **51**, 4211 (1995).

[63] A. N. Cleland, Thermomechanical noise limits on parametric sensing with nanomechanical resonators, New J. Phys. **7**, 235 (2005).

[64] O. Chubar, P. Elleaume, and J. Chavanne, A three-dimensional magnetostatics computer code for insertion devices, J. Synchrotron Radiat. **5**, 481 (1998).

[65] G. P. Berman, V. N. Gorshkov, D. Rugar, and V. I. Tsifrinovich, Spin relaxation caused by thermal excitations of high-frequency modes of cantilever vibrations, Phys. Rev. B **68**, 094402 (2003).

[66] D. Mozyrsky, I. Martin, D. Pelekhov, and P. C. Hammel, Theory of spin relaxation in magnetic resonance force microscopy, Appl. Phys. Lett. **82**, 1278 (2003).